An Optoelectronic Interconnection for Bidirectional Transmission of Biological Signals

VALERIO ANNOVAZZI-LODI AND SILVANO DONATI, MEMBER, IEEE

Abstract—**We present the analysis and design of an optoelectronic transceiver for bidirectional communication between a live laboratory animal and a fixed measurement instrument. The transceiver is based on diffuse infrared radiation and operates even without direct sight of transmitter and receiver. The communication channel is first analyzed in terms of parameters such as attenuation, bandwidth, and S/N ratio. Then we consider multiplexing and modulation schemes and discuss the design of circuits used in the miniaturized battery-operated mobile unit. Examples of experimental *in vivo* measurements of brain metabolites are finally presented.**

I. Introduction

PROPAGATION via diffused infrared radiation is a data communication channel with distinct advantages in a number of indoor applications and has been considered or proposed for office data links [1], spacecraft man-to-machine transmission [2], and laboratory biological signal links [3]. Basically, the technique is implemented by means of a LED transmitter and a photodiode (PD) receiver, and has an adequate sensitivity to allow operation without direct sight (i.e., only based on laboratory wall diffusion) in short range (several meters) and medium bandwidth (up to 1 MHz) applications [1], [3].

For biological signal transmission the technique offers a high level of electromagnetic immunity (EMI) since both radio interference and wiring-induced disturbances are avoided. Also, wire suppression is an important feature to minimize perturbations of the live animal behavior, especially in neurological experiences.

In this paper, we first present an analysis of the diffuse-light transmission channel, and derive the equations relating S/N ratio, transmitted power, and receiver area to working distance and ambient illumination. Then, we discuss the choices of multiplexing schemes, such as wavelength (optical), frequency (electrical), or time division multiplexing for the bidirectional duplex data transmission. Also, the selection of modulation and encoding techniques suitable for the optoelectronic approach is discussed. Finally, we present the design of the low-voltage, low-power circuit needed for battery operation aiming to the specific application of *in vivo* polarography on which we report experimental illustrative data.

Manuscript received June 30, 1987; revised February 22, 1988. This work was supported by CNR-CCTE.

The authors are with the Dipartimento di Elettronica, Universita di Pavia, Pavia, Italy.

IEEE Log Number 8821510.

II. Analysis of the Diffused Radiation Channel

In this section, we evaluate the propagation channel parameters, namely:

1) the static *attenuation* ratio P_r/P_t of received to transmitted powers

2) the *bandwidth* B associated with the multipath diffuse propagation.

We schematize the diffuse radiation channel as in Fig. 1: units 1 and 2 will double as transmitter and receiver in an actual optical transceiver, but for the moment let us assume a transmission from unit 1 to unit 2.

While the problem is easy to solve in regime of single diffusion, the case of interest where the *field of view* (fov) and the *field of illumination* (foi) overlap and the single diffusion yields the main contribution to the received flux P_r, the general regime of multiple diffusion through walls and ceiling is very difficult to treat analytically. However, the power contributions rapidly decrease with increasing order of diffusion and, therefore, from the application point of view, it is adequate to limit ourselves to the first-order term.

Now, let us evaluate the received power P_r for partially overlapping foi and fov as in Fig. 1, first for a static transmission. Let the optical transmitter emit a radiant flux P_t with an assigned distribution $c_i(\theta)$ within the foi, the ceiling or walls of the laboratory receive the emitted radiation and diffuse it back with a diffusivity δ, and the receiver look at the ambient with a relative sensitivity $c_f(\theta')$ within the fov, which eventually overlaps the foi, collecting a radiant flux P_r through its active aperture of area A_r. From geometrical optics, the radiance R_c of the elementary surface dA_c of the ceiling, illuminated at the off-axis angle θ by a beam of uniform distribution $c_i(\theta)$ in the solid angle $\Omega_{\text{foi}} \cong \pi(\theta_{\text{foi}})^2$ is found as

$$R_c = (\delta/\pi)(P_t/\Omega_{\text{foi}} H^2) \cos^3 \theta \qquad (1)$$

where P_t is the total radiant flux of the beam, H is the ceiling height and the factor $\cos^3 \theta$ accounts for the projection of a uniform beam on a plane surface [4]. The received power P_r can then be written, by Lambert's law as the integral of elementary contributions, i.e.,

$$dP_r = R_c \, dA_c \, d\Omega_r \cos \theta', \qquad (2)$$

which are emitted by the diffusing area dA_c within the solid angle $d\Omega_r$ subtended by the receiver. To allow for a non-

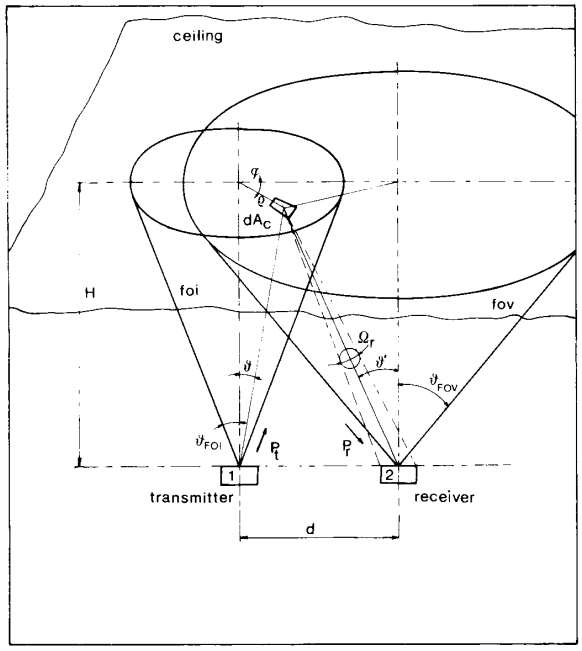

Fig. 1. Schematics of the optoelectronic diffused-radiation channel.

ideal receiver, we should multiply the right hand side of (2) for the relative angular sensitivity $c_f(\theta')$ of the receiver ($c_f(\theta') = 1$ for an ideal receiver). Thus we have

$$P_r = \int_{Ac} \int_{\Omega r} R_c \, dA_c \, d\Omega_r(\theta') \cos\theta' \, c_f(\theta'). \quad (3)$$

Using spherical trigonometry to explicitly write the terms in (3), we get

$$dA_c = H^2(\sin\theta/\cos^3\theta)\, d\theta\, d\varphi \quad (4)$$

$$d\Omega_r = dA_r \cos\theta'/L^2 = dA_r \cos^3\theta'/H^2 \quad (5)$$

and by integrating on Ω_r, we obtain

$$P_r = (\delta/\pi)(P_t A_r/\Omega_{\text{foi}} H^2) \int_0^{2\pi} d\varphi \int_0^{\theta_{\text{foi}}} \sin\theta \cos^4\theta' \, c_f(\theta')\, d\theta \quad (6)$$

where θ' is related to θ and φ by the expression

$$\tan^2\theta' = \tan^2\theta + (d/H)^2 - 2(d/H)\tan\theta\cos\varphi \quad (7)$$

d being the lateral displacement (Fig. 1). Equations (6) and (7) allow in principle to calculate exactly the attenuation of a diffuse transmission, but are difficult to solve in closed form. However, in the case of moderate foi (i.e., $\Omega_{\text{foi}} < 1$ sr), a good approximation is obtained by neglecting the variation of θ' in the entire foi, i.e., by assuming $\theta' \cong$ constant, $\tan\theta' = d/H$, so that (6) can be simplified to

$$P_r/P_t = (\delta/\pi)\left(A_r/H^2(1 + d^2/H^2)^2\right) \cdot c_f(a\tan d/H)\eta_s \quad (8)$$

where η_s is the fraction of the foi spot on the ceiling overlapped by the fov. In direct sight, if the transmitter were placed on the ceiling at $\theta = 0$ and aimed to the receiver, the power attenuation would have been

$$P_r/P_t = \left(A_r/H^2(1 + d^2/H^2)^{3/2}\Omega_{\text{foi}}\right) c_f(\text{atan}\, d/H). \quad (9)$$

Thus, the power penalty of the diffused channel with respect to a direct-sight channel is given for small lateral displacement $d \ll H$ by three factors: 1) the radiance reduction $\Omega_{\text{foi}}/\pi \cong \theta_{\text{foi}}^2$, 2) the imperfect diffusion δ, and 3) the incomplete overlap of foi and fov (η_s). Moreover, as indicated by (8), the power attenuation P_r/P_t scales as H^{-2} (for $d \ll H$ or d/H = constant) or as d^{-4} (for $d \gg H$ or H = constant) when the fov completely overlaps the foi ($\eta_s = 1$); the decrease is even faster when the overlap is incomplete ($\eta_s < 1$).

In Fig. 2(a), the attenuation P_t/P_r is plotted versus the lateral displacement d for some values of H in the case of complete overlap $\eta_s = 1$. Fig. 2(b) gives the diagram of the attenuation due to incomplete overlap η_s as a function of $d/(H\tan\theta_{\text{foi}})$ and for some typical values of the ratio $k = \tan\theta_{\text{fov}}/\tan\theta_{\text{foi}}$.

As regards to the impulse response of the optoelectronic diffuse channel, one can see by inspection of Fig. 1 that the time delay τ of the elementary contribution dA_c for the path connecting transmitter and receiver at the angles θ and θ' is given by

$$\tau = \tau' + \tau'' = (H/c)(1/\cos\theta + 1/\cos\theta') \quad (10)$$

where c is the speed of light.

Consequently, the time dependence of elementary received power dP_r when the transmitted power P_t is a Dirac impulse $D(t)$ of amplitude E_t:

$$P_t = E_t D(t) \quad (11)$$

can be written as an extension of (1) and (2), i.e.,

$$dP_r(t) = (\delta/\pi)(E_t D(t-\tau)/\Omega_{\text{foi}} H^2) \cdot \cos^3\theta \, dA_c \, d\Omega_r \cos\theta' \quad (12)$$

where the corresponding expressions of dA_c and $d\Omega_r$ [(4) and (5)] now read

$$dA_c = H^2(\sin\theta/\cos^3\theta)\, J(\theta, \varphi; \tau', \tau'')\, d\tau'\, d\tau'' \quad (4')$$

where J is the Jacobian determinant of θ, φ respect τ', τ'' as set by (10) and (7), and

$$d\Omega_r = dA_r H/(c^3(\tau'')^3) \quad (5')$$

so that one obtains as the counterpart of (6)

$$P_r(t) = (\delta/\pi)(E_t A_r H/\Omega_{\text{foi}} c^3) \iint d\tau'\, d\tau'' \cdot D(t-\tau'-\tau'')\left[1 - (H/c\tau')^2\right]^{1/2} \cdot J(\theta, \varphi, \tau', \tau'')(\tau'')^{-4} c_f(\tau''). \quad (13)$$

By solving (13) one can obtain the impulse response of the diffused light channel, i.e., a complete characteriza-

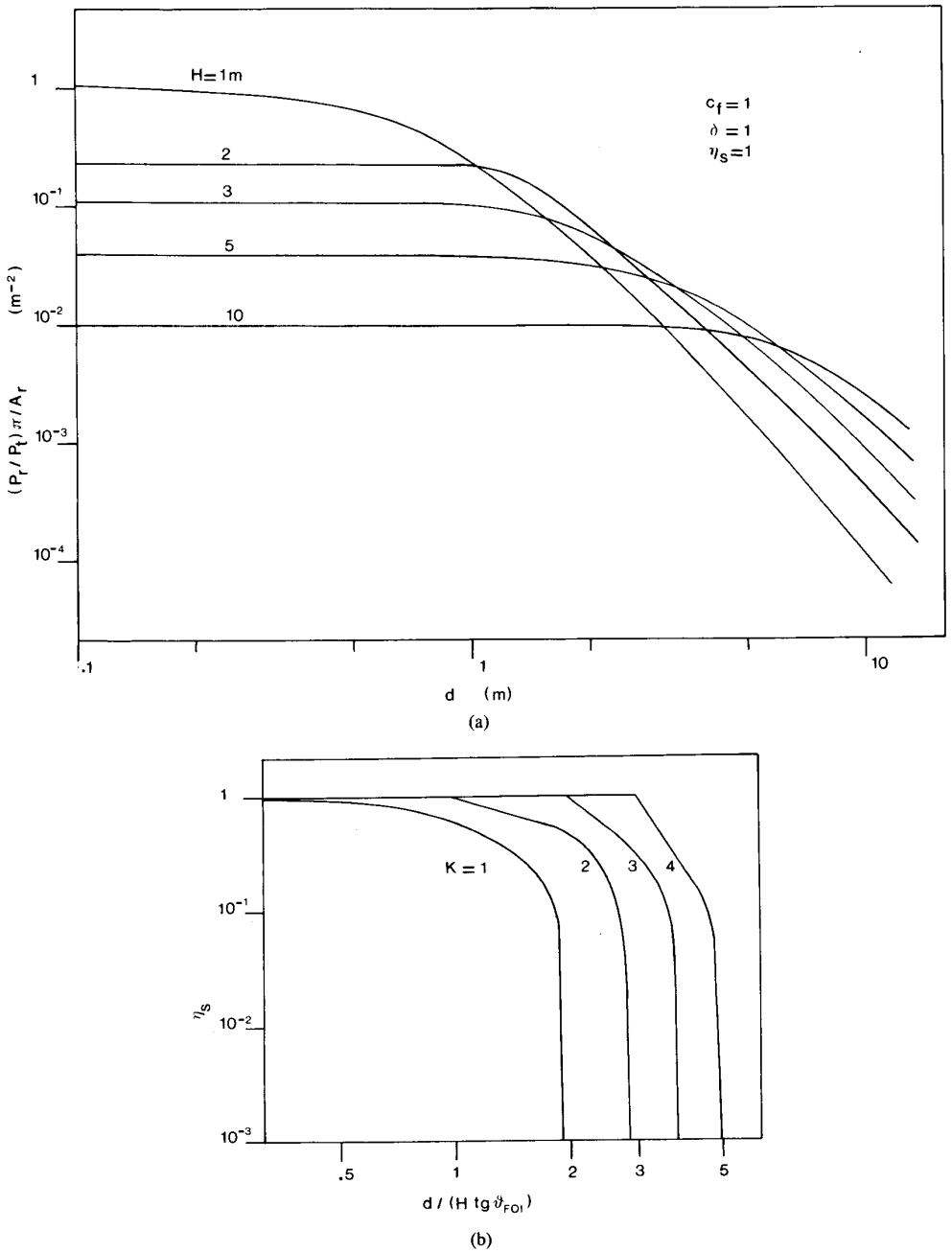

Fig. 2. Normalized collected power (a) and reduction factor η_s (b) as a function of lateral displacement d.

tion which includes the mean propagation delay time and the bandwidth. However, in the general case, (13) is difficult to treat in exact form and therefore we limit ourselves to the approximate solution in the case of moderate lateral displacement $d/H \ll 1$ and complete overlap of fov over foi. Then, (13) can be evaluated as follows:

$$P_r(t) = \begin{cases} (\delta E_t A_r/\Omega_{\text{foi}})\, H^3/\left(c^5(t/2)^6\right) & \text{for } \tau_1 < t < \tau_2 \\ 0 & \text{elsewhere} \end{cases} \quad (14)$$

where

$$\tau_1 = 2H/c \qquad \tau_2 = 2H/(c \cos \theta_{\text{foi}}) \quad (15)$$

$$\Delta\tau = 2(H/c)\left((1 - \cos \theta_{\text{foi}})/\cos \theta_{\text{foi}}\right) \quad (16)$$

The impulse response $P_r(t)$ given by (14) is plotted in Fig. 3 for some values of θ_{foi}; as expected, it starts after a propagation time delay τ_1 with respect to the emission and decreases as an inverse power of time till the maxi-

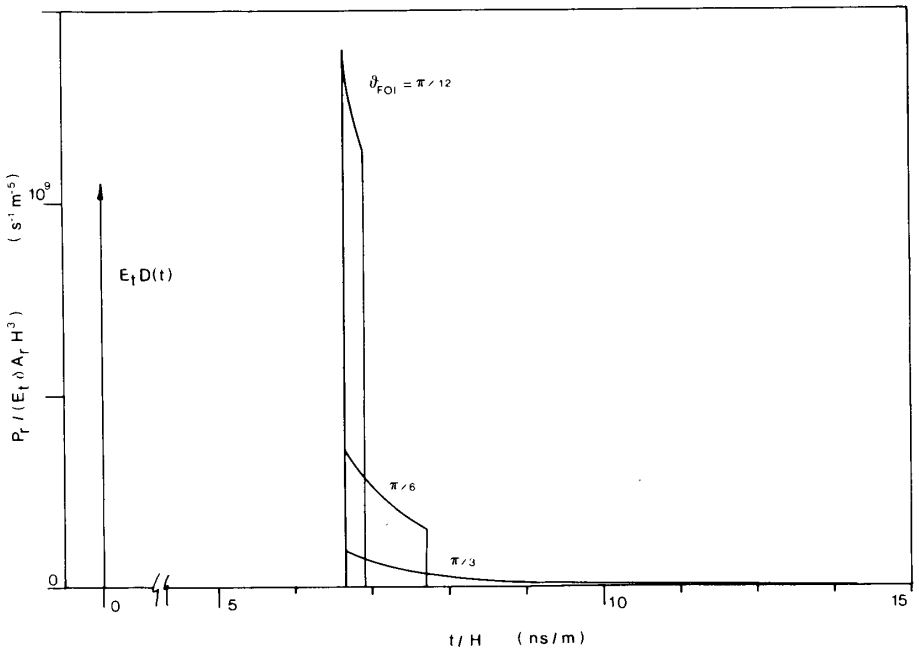

Fig. 3. Normalized impulse response of the diffused channel.

mum propagation delay τ_2. Also, the maximum value of the impulse response i.e., at $t = \tau_1$ is found from (14) as

$$P_r(\tau_1) = (\delta E_t A_r/\Omega_{foi})\, c/H^3 \qquad (17)$$

and the time duration of the impulse response is equal to $\Delta\tau = \tau_2 - \tau_1$ as given by (16), showing the dependence on the aperture of the field of illumination Ω_{foi}. Incidentally, we note that when $\theta_{fov} < \theta_{foi}$, the shape of the impulse response is unchanged; equations (15), (16) still hold if θ_{foi} is substituted by θ_{fov}, and the amplitude is scaled by the factor $\eta_s < 1$. These results should be compared to those found by Bapst and Gfeller [1] under a different approach, i.e., by assuming the ceiling as a diffusing source of Lambert radiance. In our notation, we can derive this result by neglecting τ' in (13), so that $\Delta\tau$ is halved and the time dependence of $P_r(t)$ is as t^{-3} [1] instead of t^{-6}, i.e.:

$$P_r(t) = (2\delta E_t A_r/\Omega_{foi})(1/c^2 t^3)$$
$$\tau_1/2 < t < \tau_2/2. \qquad (18)$$

As regards the bandwidth available with the diffuse light channel, we can evaluate it according to the usual definition as the -3 dB frequency of the modulus of the Fourier-transform $F(P_r(t))$. The exact result of this calculation is rather involved and it is not reported here; however, we quote the good approximation which is obtained for small θ_{foi}, so that τ_1 and τ_2 are comparable and the impulse response $P_r(t)$ can be assumed of rectangular shape. Accordingly, the bandwidth B is given by

$$B = 0.44/\Delta\tau = (0.22\, c/H) \cos\theta_{foi}/(1 - \cos\theta_{foi}). \qquad (19)$$

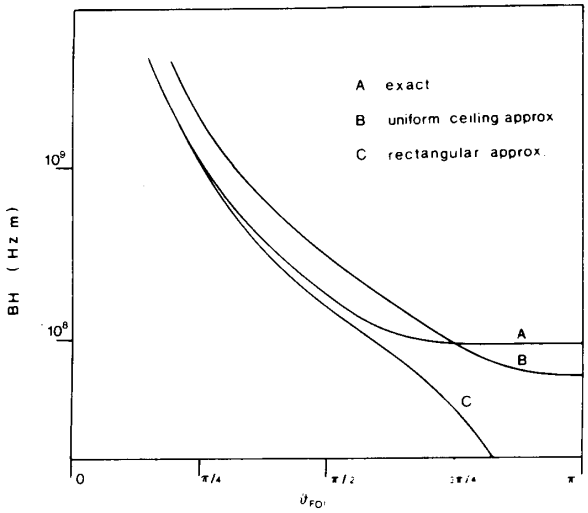

Fig. 4. Diffused channel bandwidth-distance product as a function of θ_{foi}.

As an example, for $\theta_{foi} = \pi/6$ we get from (19) a constant bandwidth-height product $BH = 427$ MHz · m. Thus, a bandwidth of at least several tens MHz is in principle available in typical laboratory conditions.

In Fig. 4 we compare the approximate result given by (19) to the exact one which is obtained by solving (14). Also, we report the bandwidth dependence as evaluated numerically from (18) (one way diffuse link [1]). In all cases, the bandwidth-height product BH turns out to be

independent from H. As it can be seen, a good approximation is supplied by (19) for $\theta_{foi} < \pi/3$ while the factor 2 of increase with respect to the result of (18) simply comes from the halfway propagation considered in [1].

Finally, we note that for $\theta_{fov} > \theta_{foi}$ the results of Fig. 4 still hold, assuming θ_{fov} instead of θ_{foi} on the abscissa.

III. Choice of Photodetectors and Emitters for an Optoelectronic Link

In order to find the parameters of sources and detectors to be optimized, let us now derive an expression for the S/N ratio at the receiver front-end amplifier.

The photogenerated signal current on the photodiode array can be written as

$$I_s = \sigma P_r$$

where σ is the spectral sensitivity (A/W), or equivalently by using (8) as

$$I_s = \sigma A_r K P_t \tag{20}$$

where K is given by

$$K = (\delta/\pi)\, c_f \eta_s / L \tag{21}$$

and the factor L, i.e.,

$$L = H^2(1 + d^2/H^2)^2, \tag{22}$$

summarizes the geometrical factors.

The noise superposed on the signal current arises from different contributions:

1) shot noises associated with signal current I_s, dark photodiode current I_D, and ambient stray-light photogenerated current I_L.

2) Johnson noise associated with the load resistor R of the photodetector.

3) input equivalent noises of the preamplifier i_n and v_n.

In most practical cases, where a moderate amount of background illumination is present, and a proper preamplifier design is ensured, the contribution of I_L dominates and

$$I_N = (2qI_LB)^{1/2} \tag{23}$$

where B is the amplifier bandwidth and q is the electron charge. Therefore, we get for the S/N ratio

$$S/N = (\sigma K P_t \sqrt{A_r})/(2q\sigma^* EB)^{1/2}. \tag{24}$$

Here, I_L has been expressed in terms of the ambient illumination E, the device area A_r, and its responsivity σ^* (A/lm). Equation (24) shows that to improve system performances either the emitted power P_t or the collecting area A_r should be increased.

In a bidirectional transmission system intended to perform a link between a main instrument and a satellite mobile unit, the satellite transceiver usually requires low power and compact design while in the main one larger power consumption and dimensions are acceptable. Therefore, it is advisable to use high-power LED's and large area photodiodes on the main transceiver and high-efficiency LED's, high-responsivity photodiodes on the satellite.

Since a real photodiode is limited by the parasitic capacitance C which reduces the maximum frequency of operation $1/2\pi RC$ where R is the effective load of the photodiode, the figure of merit to be optimized is the A_r/C ratio. When a large collecting area is required it may be better to divide the photodiodes into small groups, each with an individual front-end amplifier.

To alleviate for stray-light effects, optical filters can be introduced in front of each photodiode. In this case, the dark current contribution to shot noise can be comparable to I_L and the photodiode must be chosen so as to minimize the I_D/A_r ratio.

Optical elements can be used on the light-emitter to tailor the emission angle (θ_{foi}) and on the detector to increase its effective collecting area A_e or its field of view (θ_{foi}). Obviously, these quantities cannot be both increased once the photodiode area A_r is fixed since

$$A_r = A_e \sin^2(\theta_{foi}) \tag{25}$$

for an ideal concentrator as a consequence of the principle of radiance invariance. From (8) and Fig. 1 it is advisable to choose θ_{fov} and θ_{foi} so that the receiver field of view completely intercepts the transmitter spot on the ceiling for any practical relative position. However, a large value of θ_{fov} greatly increases the collected stray light while a very small value of θ_{foi} may cause transmission failure due to obstacles in the room.

Sources and emitters are available at different wavelengths of operation. If optical multiplexing is not necessary, it is reasonable to operate at $\lambda = 950$ nm where p-n silicon photodiodes reach their maximum responsivity and high-efficiency GaAs LED's are available. Low-cost implementation is possible at this wavelength using large area silicon p-i-n photodiodes and GaAs LED's in plastic case. Modulation frequency up to about 1 MHz is easily achieved. When optical multiplexing must be used, other channels can be implemented at a higher cost, e.g., at $\lambda = 850$ nm, using silicon photodiodes, GaAlAs LED's, or at $1.1 \div 1.5$ μm, using Ge p-n or p-i-n photodiodes and InGaAsP LED's. Though high radiance is not necessary in this application, laser diode sources are the only possible alternative to LED's when a great number of separate optical channels are required.

A quick evaluation of the system performance can be obtained using the nomogram of Fig. 5. Indeed, by combining (20)–(24) one can find a relationship between signal and noise currents I_s and I_n, transmitted power P_t, distance L, collecting area A_r, bandwidth B, and ambient illumination E:

$$I_s = I_s(P_t, L; A_r, \sigma)$$

$$I_N = I_N(E, B; A_r, \sigma^*).$$

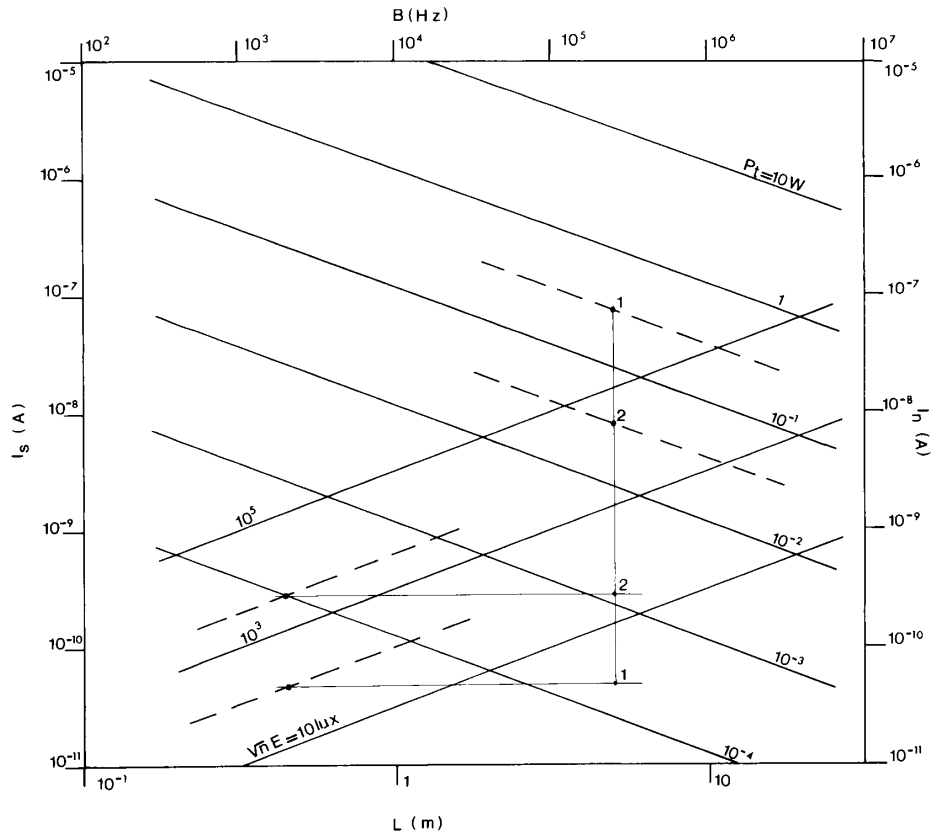

Fig. 5. Nomogram for S/N evaluation of the diffused link.

The nomogram can be used, for example, by entering first the values of power P_t and equivalent distance L [(22)] to find the received signal I_s; then entering the values of E and B to find I_N and finally getting the signal-to-noise ratio

$$S/N = I_s/I_N$$

as the distance along the ordinate of the nomogram. The nomogram has been drawn for $\delta = 1$, $c_f = 1$, $\eta_s = 1$ and assuming the parameters of the devices used in our design (see Section VII), i.e.: $A_r = 7$ mm^2, $\sigma(\lambda = 950\text{ nm}) = 0.57$, $\sigma^* A_R = 3.3\ 10^{-8}$ A/lux. The last value has been computed for a blockbody spectrum at $T = 2850$ K and is in agreement with measurements performed with commonly used tungsten lamps.

IV. Multiplexing Schemes

For the transmission of several signals in the optoelectronic channel, one shall resort to a multiplexing scheme. Several choices of multiplexing (mpx) are available of which the most interesting are

1) wavelength (optical) mpx,
2) frequency (electrical) mpx, and
3) time division (electrical) mpx.

Wavelength mpx can be accomplished in two ways: by using separate wavelength sources, one for each channel, or by splitting the wavelength spectrum of a single source. In both cases, to recover each channel one employs an individual narrow-band filter in front of each photodetector.

By referring to commercially available LED's, one can allocate up to $n = 6$ channels in the wavelength range 820–1500 nm where high-efficiency devices exhibit typical spectral linewidths of less than 100 nm at 5 percent of the peak amplitude. In view of these wavelength intervals, the filter specifications are not particularly demanding. Obviously, many more channels (e.g., up to $n = 20$) can be allocated with the use of laser diode sources.

The second wavelength mpx scheme, proposed [1] and best suited for the high efficiency LED's at $\lambda = 950$ nm, consists in splitting the relatively broad linewidth of the source in a few channels by means of interference filters. Although feasible in principle, this approach requires

carefully designed and steep-response filters which offset the cost benefit of the source.

Frequency-domain electrical mpx can be implemented using a number of subcarriers (one for each channel) which modulate in amplitude the LED optical emission. The channel allocation must be in a frequency range higher than, say, 1 kHz to avoid interference from lamps and fluorescent tubes and lower than the 3 dB cutoff B of either the LED frequency response or the optoelectronic channel bandwidth (Section II). If the signal bandwidth occupation is B_s, it turns out that the number of separate channels available with frequency mpx is $n = B/B_s$.

Time division mpx requires sampling, and usually coding, of the signals to be transmitted on the same carrier. Syncronism information must be provided at the receiver to reconstruct signal through decoding and holding. In principle, the number of channels is about the same as for frequency multiplexing.

For bidirectional transmission, a variant of time division mpx, i.e., *ping-pong* mpx, allows us to save bandwidth when a quasi-full-duplex link can match design specifications. In this case, the same channel is used alternatively for transmission in both directions, while timing circuits located on one apparatus (the main) control the channel access. In a first phase, the main unit transmits data to the satellite receiver. The last word is recognized by the satellite as an order to switch to transmission for a specified time while the main waits for data to receive (second phase). After this time is elapsed, phase one is restarted. This kind of mpx requires little additional circuitry on the satellite since the main unit support timing and sinchronisation. During the first phase the transmitter on the satellite can be switched off, thus allowing to reduce power consumption, which is a distinct advantage especially for battery-operated optoelectronic transmitters.

V. Modulation and Coding

The optical carrier generated by the LED array is easily modulated in amplitude through the driving current. Information can be transmitted directly by baseband modulation or using an electrical subcarrier. However, this scheme is very sensitive to environmental sources emitting modulated light with frequency components falling within the receiver passband. Therefore, information redundance should be introduced. Baseband multichannel transmission can be performed using synchronous PWM or by optical multiplexing.

The use of electrical subcarries (one for each channel) modulating in amplitude the optical carrier is a more suitable approach. Phase or frequency modulation should be used on the subcarries since, as it is well known, amplitude modulation is more sensitive to additive noise and does not retain the scale factor information. We have used square-wave frequency modulation of the uncoded analog signal with a straightforward voltage to frequency conversion scheme, as detailed in Section VII. This approach allows easy implementation and low-component count; in addition it improves power efficiency since the LED source is driven in pulsed regime. Obviously, channel allocation must be carefully studied so as to avoid crosstalk due to harmonic components of the square wave subcarries.

More sophisticated approaches can be considered where high compactness is not a goal, including processing of the modulating signal, or sampling and digitalization (PWM, PCM).

VI. Optoelectronic Transceiver for Polarographic Experiments

Polarography is a well-known technique [5], [6] which allows us to detect chemical species in a solution and to measure their concentration. Besides its applications in organic and inorganic chemistry, polarography is extensively used in the medical and biological fields. In neurochemical studies, it allows the determination of brain metabolites, e.g., 3–4 dihydroxyphenilacetic acid (DOPAC) and 5-hydroxyindolacetic acid (5-HIAA), down to $10^{-8} \div 10^{-10}$ M sensitivity.

A conventional experimental setup is shown in Fig. 6(a): a slow-varying voltage ramp V is applied to the cell by means of two electrodes and the current through the cell is recorded. A diagram of I versus V (polarogram) is obtained as in Fig. 6(a) where each plateau represents the saturation (diffusion limited) oxidation current ΔI_a of a ion, proportional to concentration, while the abscissa V_a gives the oxidation potential from which the chemical species can be identified.

This basic scheme can be improved in a number of ways, depending on the specific application. In Fig. 6(b) we report the experimental setup for three-electrode pulse polarography, i.e., a viable technique for *in vivo* determination of catecholamines [7], [8]. A few years ago *in vivo* monitoring of the levels of DOPAC and 5-HIAA has been demonstrated [7], [9], thus allowing to study directly the metabolic activity of neurons.

The voltage ramp, which typically ranges from -200 to $+200$ mV in a 40 s scan time, is applied to the cell (the rat brain) between the reference and the work electrode. The former is a Ag/Ag Cl system whose potential is known and stable. The latter is a carbon fiber electrode chemically treated [7], so as to enhance its responsivity and selectivity between the chemical species of interest (e.g., DOPAC versus ascorbic acid). The third (auxiliary) is a platinum electrode which allows, in connection with the operational amplifier, to keep constant the voltage V irrespective of brain impedance. Also, this configuration avoids current I, which typically ranges from 1 to 100 nA, from passing through the reference electrode whose electrochemical properties would otherwise rapidly degrade.

The voltage waveform carries a series of pulses ($20 \div 40$ ms in duration, 20–60 mV in amplitude). The oxida-

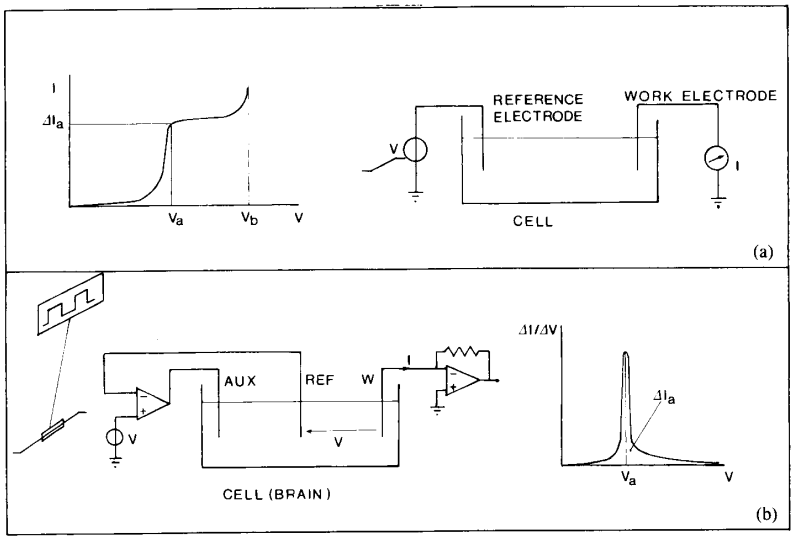

Fig. 6. (a) Basic scheme of a polarographic determination. (b) Three-electrode pulse polarography.

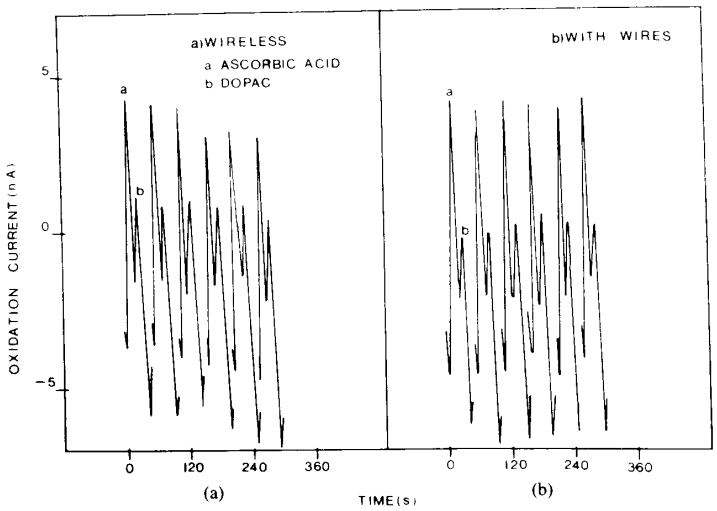

Fig. 7. Determination of DOPAC and 5-HIIA (a) by the optoelectronic transceiver and (b) with wires.

tion current is obtained as the difference between the current sampled after a fixed delay from the pulse leading edge (so that the current component due to interelectrode capacitance is negligible) and that sampled immediately before the pulse. Straightforward signal processing then gives the well readable diagram of Fig. 6(b) where each species is represented by a peak the area of which is proportional to concentration.

This technique has advantages in S/N ratio and selectivity [7] and increased electrode lifetime. For such experiments, a three-wire connection through coaxial cables is required between the laboratory animal and the measuring instrument (polarograph).

To allow experiences in which the animal is freely-moving, we have employed an optoelectronic transmission system consisting of a mobile unit, mounted on the rat and of a fixed unit, connected to the polarograph. The system has been routinely used for determination of 5-HIAA and DOPAC on rats.

Figs. 7 and 8 show a comparison between wire and optoelectronic experiments. Fig. 7 shows polarograms obtained *in vivo* on the same rat sweeping the potential range from -200 mV to $+200$ mV. The shape of the two peaks (DOPAC and ascorbic acid) is not distorted by transmis-

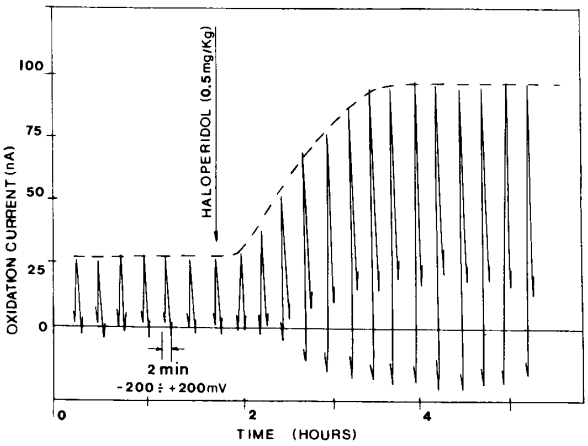

Fig. 8. *In vivo* determination of DOPAC in a rat brain using the optoelectronic transceiver. The response to injection of a drug is shown.

sion; moreover, a little improvement in S/N ratio has been gained because of the better electromagnetic compatibility of the IR link as compared to the wire connection.

This measurement is relative to a brain area not sensitive to stress (striatum) and has been chosen for comparison. However, the optoelectronic link is attractive especially when working on brain areas where a stress condition can affect metabolite levels. Fig. 8 reports monitoring of the DOPAC level in such an area (nucleus accumbens) after injection of a drug. A relative increase of 300 percent is found as expected and the peak shape and height are quite unaffected by ambient disturbances.

VII. Circuit Design and Performances

We show in Fig. 9 the block scheme of the two-way transceiver as connected for *in vivo* three-electrode pulse polarography. The main unit transmits the slow pulse ramp generated by the polarograph to the mobile unit located on the rat. The receiver converts the infrared signal and applies the voltage ramp to the electrodes implanted in the rat brain. The response current is amplified and the signal is sent back to the polarograph via the return channel, thus getting information on the concentration of brain metabolites.

Square-wave voltage to frequency conversion has been used and electrical multiplexing has been implemented with 8 kHz (first channel) and 80 kHz (return channel) subcarriers. The optical carrier is at $\lambda = 950$ nm for both channels for best LED efficiency (≈ 10 percent) and LED/photodiode matching.

A 16-LED array (Siemens LD 271, $\Delta\lambda = 50$ nm, CW power output $P_t = 16$ mW) and a six-photodiode array (Siemens SFH 205, $A_r = 7$ mm^2) has been used on the main unit, while single components are mounted on the satellite. The photodiode has a built-in color filter ($\Delta\lambda =$ 190 nm) which allows to reduce the collected stray light that could otherwise saturate the front-end amplifier. The rejection ratio depends on wavelength, i.e., on the spectral distribution of the background illumination. It has been found experimentally that the filtering action is quite poor for tungsten lamps ($T = 2300 \div 2850$ K), where the reduction is less than 50 percent, while it is better for the sun (about a factor 5), and very good for fluorescent lamps (a factor 10). This last feature is of help since fluorescent lamps are rich in high-order harmonics which would disturb the receiver and reduce S/N ratio. Though the color filter improves operation, it may not be sufficient alone: e.g., for a background illumination $E = 1000$ lx the photogenerated current without the color filter is

$$I_L = n\sigma^* A_r E \tag{26}$$

and for a tungsten lamp source ($\sigma^* A_r = 5.10^{-8}$ A/lux) I_L can be as high as 300 μA, while the signal can be down to 1 nA, thus saturating the front end amplifier if $R > 100$ kΩ and $Vcc \leq \pm 15$ V.

As stated above, the color filter improves this limit only by a factor two, but a further improvement in the rejection of stray light effects is desirable and it has been introduced by an electronic feedback loop implemented around the front-end amplifier, a well known cold resistance scheme (see Fig. 10). A current generator acts so as to sink the photogenerated current in a band from dc to 500 Hz. The effect of sun and lamps, including neon tubes, is therefore cancelled at the expense of a 3 dB deterioration of S/N ratio.

An additional source of disturbances, i.e., electromagnetic interference (EMI) may be of importance. To achieve a high level of EMI immunity, a dummy wiring with 6 MΩ resistances (a value equal to the differential resistance of the photodiodes) has been laid in close proximity to each photodiode and connected to the noninverting input of the op-amp [3]. Since the dummy load collects nearly exactly the same electrical interference as the photodiodes, the two contributions cancel each other at the op-amp output (see Fig. 10). While giving a little contribution to the total noise, this cancellation technique was found adequate. In a typical laboratory environment, the disturbances are usually much larger than the achievable noise, set by (23), and it is impractical to shield the photodiodes without shadowing them. In typical operating conditions the S/N ratio was increased about 30 dB with this cancellation scheme.

The front-end amplifier has been designed so that the major noise contribution is given by the photodiode shot noise even for very small levels of background illumination E [(23)]. The noise contribution of the feedback resistance R amounts to

$$I_{NR} = (4kTB/R)^{1/2} \tag{27}$$

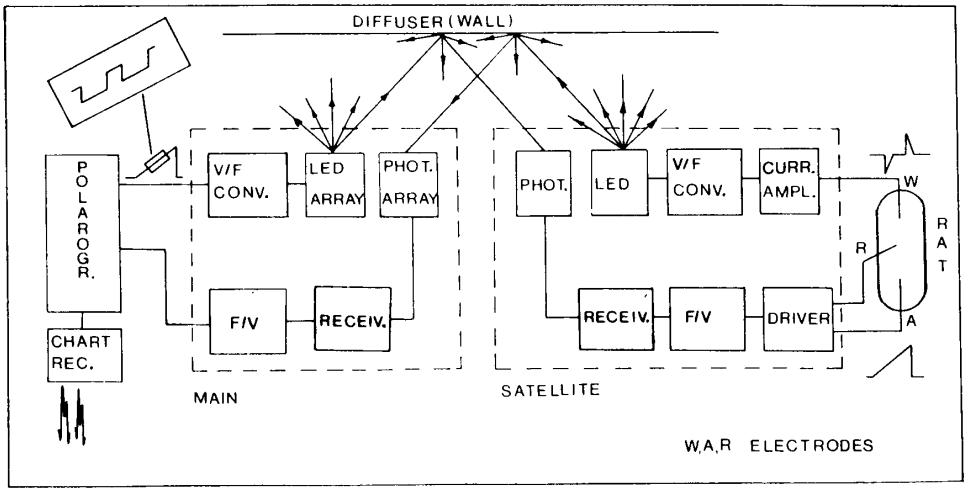

Fig. 9. Block scheme of the optoelectronic transceivers (main and satellite) as connected for three-electrode pulse polarography.

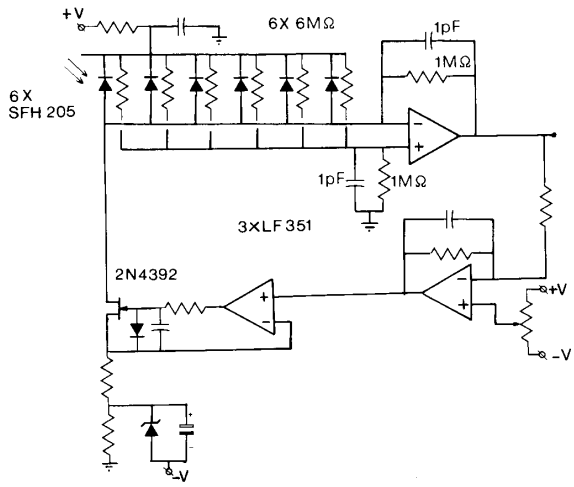

and shall be calculated for $B = 2$ kHz, a value given by the carrier filter, and $R = 1$ MΩ, a resistance value compatible with bandwidth requirements. It is then found $I_{NR} = 7$ pA. Neglecting the op-amp and the cancellation network contribution, we find from (23) that the comparable noise source is an illumination level as low as $E = 1$ lx. In the dark, typical noise equivalent level (NEI) measured on the main unit are $I_N = 0.45\ \text{pA}/\sqrt{\text{Hz}}$ for each photodiode, about four times the Johnson's contribution due to resistance R; this is due to the op-amp input noise current.

The electrical scheme of the satellite unit is reported in Fig. 11. It requires two thin Li batteries (± 3 V) for a few hour's operation. The major contribution to the current drain is due to the LED driving (10 mA) though duty cycle has been reduced to 20 percent. The constraint of low-voltage, small area forced to use bipolar quad op-amps of relatively small gain-bandwidth product. Symmetrical FET source followers have been introduced where low-bias current, high impedance is mandatory, i.e., in the current amplifier and in the cell driver. A cancellation scheme is used also in the front end of the satellite. The NEI is about a factor two greater than in the main unit.

The above described transceiver system performs a link in the range of some meters depending on the optical characteristics of the room. In the typical case where the diffuser is a white wall and the stray light illumination amounts to 300 lx, good quality transmission has been performed in a range of more than five meters. Entering the nomogram of Fig. 5 with $E = 300$ lx, $B = 2$ kHz, $L = 5$ m, we find the $S/N = 60$ dB for channel 1 and $S/N = 30$ dB for channel 2. It should be pointed out, however, that the S/N ratio is improved by demodulation followed by baseband filtering so that the quality of the reconstructed signal can be even better than that of the modulated carrier. For polarographic experiments, the baseband has been limited to 100 Hz and the S/N ratio is improved to about 30 dB over the values measured on the front end.

In the present design, the system can handle signals ranging from dc to 1 kHz. A linearity error lower than 1 percent has been measured while the baseline drift is less than 10 mV during the usable battery life. A dynamic range of ± 1 V has been obtained by shifting the reference level of the current amplifier through a diode (Fig. 11) to compensate for the nonsymmetrical saturation levels of the op amps.

The satellite circuit has been implemented in surface mount technology (SMT) on a double face printed circuit board using miniaturized passive and active components (Fig. 12). For the use on small animals, the circuit can be folded in two parts with overall dimensions of 28 ×

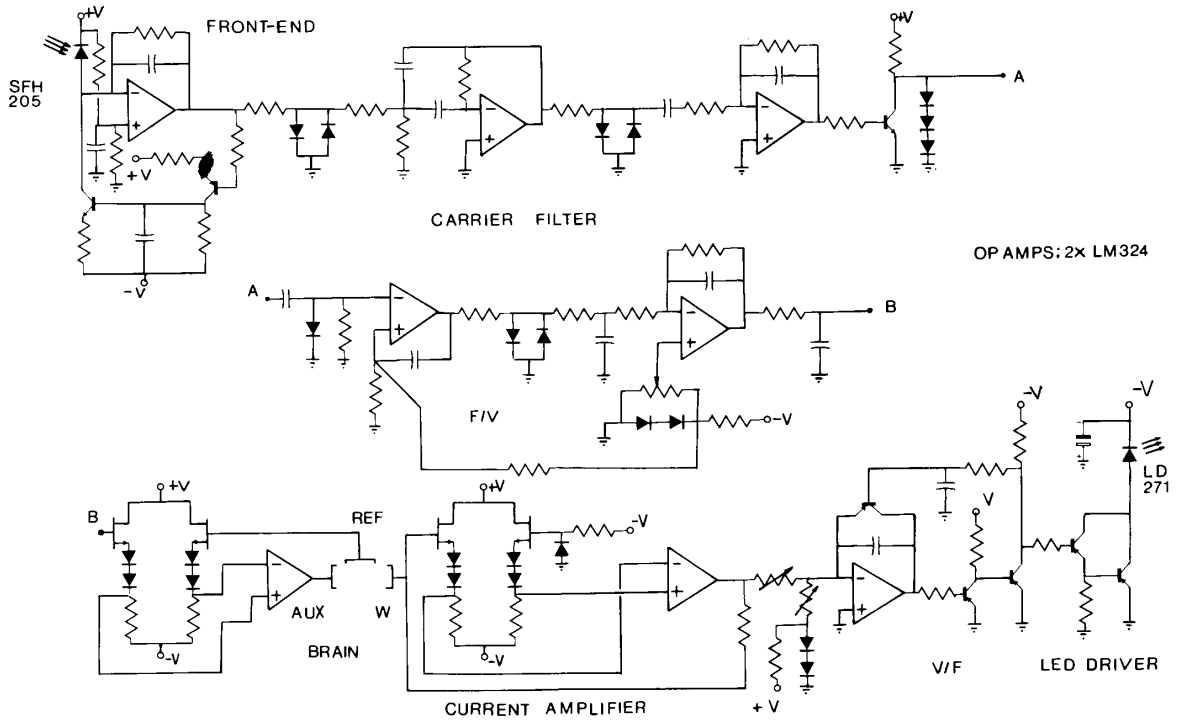

Fig. 11. Detailed electric scheme of the satellite transceiver.

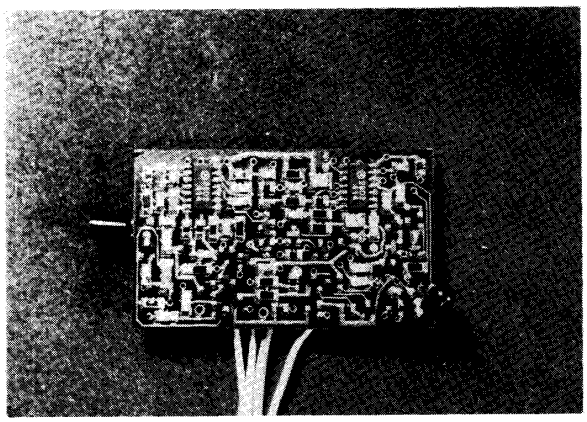

Fig. 12. Miniaturized satellite transceiver built in surface mount technology (SMT).

26 × 8 mm.

Acknowledgment

The authors thank M. Algeri and M. G. DeSimoni of the Istituto di Ricerche Farmacologiche M. Negri, Milan, for the experiments on live animals and the discussion of results.

References

[1] F. R. Gfeller and U. Bapst, "Wireless in-house data communication via diffused infrared radiation," *Proc. IEEE*, vol. 67, pp. 1474–1485, Nov. 1979.
[2] J. Grady, "Space station: Laser and electrooptics," in *Proc. CLEO-85*, Baltimore, MD, 1985, p. 108.
[3] S. Donati and G. Martini, "Design charts for optoelectronic transmission via free propagation," in *Proc. Laser 81*, Munich, 1982, pp. 434–439.
[4] A. W. Snyder and J. D. Love, *Optical Waveguide Theory*. New York: Chapman and Hall, 1983, p. 76.
[5] M. M. Pointeau and B. Bonastra, *Elements de Polarographie*. Paris, France: Masson et Cie, 1970.
[6] M. M. Zuman and C. L. Perrin, *Organic Polarography*. New York: Interscience, 1969.
[7] J. L. Ponchon, R. Cespuglio, F. Gonon, M. Jouvet, and J. F. Pujol,

"Normal pulse poloragraphy with carbon fiber electrodes for in Vitro and in Vivo determination of catecholamines," *Anal. Chem.*, vol. 51, pp. 1483–1486, Sept. 1979.

[8] L. L. Iversen, S. D. Iversen, and S. H. Snyder, *New Techniques in Psychopharmacology*. New York: Plenum, 1979.

[9] M. G. De Simoni, R. Giglio, G. Dal Toso, "Interaction between serotonergic and dopaminergic system detected in striatum by differential pulse voltammetry," *Euro. J. Pharm.*, vol. 110, pp. 289–290, Jan. 1985.

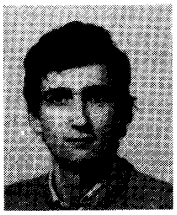

Valerio Annovazzi-Lodi was born in Novara, Italy, on November 7, 1955. He received the degree in electronic engineering from the University of Pavia, Pavia, Italy, in 1979.

Since 1979 he has been with the Department of Electronics, University of Pavia, working in the field of electrooptics on subjects such as the injection modulation phenomena in lasers, the birefringence effects in optical fibers, fiber sensors, and transmission via diffused infrared radiation. In 1983 he became a Staff Researcher at the Department of Electronics, University of Pavia.

Dr. Annovazzi-Lodi is a member of AEI.

Silvano Donati (M'75) was graduated from the University of Milano, Milano, Italy, with a degree in physics in 1966.

From 1966 to 1975 he was with CISE, working on photomultiplier and avalanche photodiode noise, nuclear electronics, image converters and LLLTV gated imaging systems, vision in scattering media, and laser telemetry. From 1971 to 1980 he was a Lecturer at the University of Pavia, Pavia, Italy. In 1981, he was appointed Full Professor of Electrooptics in 1981. He has conducted research on CCD noise, laser interferometry, coupling modulation, and reflection-induced modulation in laser oscillators, speckle-pattern statistics, and diffuse optoelectronic transmission. His main interest is now in fiber optics sensors and optoelectronic instrumentation.

Dr. Donati is a member of AEI, ISHM, APS, and OSA.